applied sciences

Article

Discrete Lattice Element Model for Fracture Propagation with Improved Elastic Response

Jadran Čarija [1], Eduard Marenić [2], Tomislav Jarak [3] and Mijo Nikolić [1,*]

[1] Faculty of Civil Engineering, Architecture and Geodesy, University of Split, 21000 Split, Croatia; jadran.carija@gradst.hr
[2] Institute Clement Ader (ICA), Université de Toulouse, CNRS-INSA-UPS-ISAE-Mines Albi, F-31400 Toulouse CEDEX 04, France; marenic@insa-toulouse.fr
[3] Institute of Advanced Production Technologies, University of Valladolid, 47011 Valladolid, Spain; tomislav.jarak@uva.es
* Correspondence: mijo.nikolic@gradst.hr

Abstract: This research presents a novel approach to modeling fracture propagation using a discrete lattice element model with embedded strong discontinuities. The focus is on enhancing the linear elastic response within the model followed by propagation of fractures until total failure. To achieve this, a generalized beam lattice element with an embedded strong discontinuity based on the kinematics of a rigid-body spring model is formulated. The linear elastic regime is refined by correcting the stress tensor at nodes within the domain based on the internal forces present in lattice elements, which is achieved by introducing fictitious forces into the standard internal force vectors to predict the right elastic response of the model related to Poisson's effect. Upon initiation of the first fractures, the procedure for the computation of the fictitious stress tensor is terminated, and the embedded strong discontinuities are activated in the lattice elements for obtaining an objective fracture and failure response. This transition ensures a shift from the elastic phase to the fracture propagation phase, enhancing the predictive capabilities in capturing the full fracture processes.

Keywords: discrete lattice element model; rigid-body spring; elastic response; embedded strong discontinuities; fracture propagation; failure

Citation: Čarija, J.; Marenić, E.; Jarak, T.; Nikolić, M. Discrete Lattice Element Model for Fracture Propagation with Improved Elastic Response. *Appl. Sci.* **2024**, *14*, 1287. https://doi.org/10.3390/app14031287

Academic Editor: Elza Maria Morais Fonseca

Received: 14 January 2024
Revised: 29 January 2024
Accepted: 1 February 2024
Published: 4 February 2024

1. Introduction

The study of fracture propagation plays an important role in engineering and materials science, providing insights into the structural integrity of materials and the behavior of complex systems under various conditions. In this context, discrete models have proved to be powerful tools for accurate representation of internal processes associated with fracture propagation [1]. These models offer the capability not only to simulate macroscale fractures and cracks but also to capture lower-scale crack propagation, including mesoscale and microscale phenomena. Among the diverse range of discrete models, classical particle discrete models such as the discrete element method [2], discrete lattice element method [1], and finite discrete element method [3] have proven particularly effective in various fields of engineering failure analysis of concrete, rocks, and other materials [4–7].

While discrete models properly capture the discontinuous nature of fracture propagation problems, they have limitations in accurately capturing the global and/or local elastic response of materials and structures [8–12]. Namely, discrete element models commonly employ one-dimensional elements such as bars, beams, or springs to simulate particle interactions, restricting their ability to capture a wide range of Poisson ratios. This leads to a mismatch between local and global elastic constants, where the elastic input parameters of the models fail to align with the overall global elastic response of the material. Consequently, these discrepancies can lead the models to generally fail in the prediction of material behavior. In this paper, we focus on improving the existing discrete lattice element models based on Timoshenko beams with embedded strong discontinuities [13,14] for the objective simulation of fracture processes by enhancing the representation of the elastic response. More precisely, our focus is on bridging the gap between local and global elastic constants, while still allowing the full failure representation of the material. In order to achieve an improved elastic response and accurate representation of the fracture propagation mechanisms, we adopt the kinematics typical of rigid-body spring models [10,11]. More precisely, such connections are considered here as generalized beam lattice elements, closely related to Timoshenko beam elements, which enable the application of a procedure for correcting the elastic response of undamaged material, as in [8,9,15,16]. Such a generalized beam lattice element is equipped with embedded strong discontinuities [17,18] for the propagation of fractures in the domain.

In the proposed approach, the stress tensor at the lattice element network nodes is computed by considering all stress resultants from the elements connected to a specific node. Subsequently, fictitious forces [8,9,19] are computed by extracting information from the transverse strains that need to be achieved. By introducing these fictitious forces in the lattice elements of the model, we ensure that the local element stiffness aligns with the global material properties, correcting the elastic response. Moreover, a wide range of Poisson ratios is possible to be achieved with this approach, which was not the case in classical discrete beam lattice models. Following this correct computation of the elastic response, fracture criteria pertaining to the maximum tensile strength and maximum shear strength are systematically checked in all elements [1]. The procedure of fictitious forces and correction of the elastic response is terminated once the first elements exhibit failure, signifying the material's progression towards a fully discontinuous state and eventual total failure. This approach aims to provide a more realistic representation of the elastic response in discrete lattice element models, while correctly capturing the complexities of fracture propagation.

The softening response represents material failure where classical finite element procedures struggle. Namely, the representation of failure with softening in traditional methods is prone to mesh dependency. Recognizing this limitation, various advanced methods have emerged to correct softening behavior. Among these, there are non-local damage and plasticity models [20–23], various localization limiters like those listed in [18], and, more recently, the very popular phase field models [24]. The extended finite element method (X-FEM) is another type of approach to address this issue, in which discontinuous functions are introduced in the formulation, while treating additional unknowns associated with fractures on a global scale [25,26]. Alternatively, the embedded discontinuity finite element method (ED-FEM) addresses the additional discontinuity-related unknowns locally at the element level [27–31]. Within our lattice element method, we adopt a solution for softening regularization by using the embedded strong discontinuity framework proposed in [17]. This involves the implementation of embedded strong discontinuities within the lattice element models, as presented in [32–36]. Here, the material parameter governing softening is the fracture energy, which enables the mesh-independent softening response. It is worth noting that alternative models utilizing the granular micromechanics damage approach with finite deformation also produce proper modelling of the localization zone [37–39], which is similar to non-local damage models. The models based on lattice structure can also be used in large-motion dynamics [40] and buckling problems [41].

The proposed novel model integrates the embedded strong discontinuity framework and previously mentioned correction of elastic response within the lattice element model aiming to fully capture the material failure. To that end, the proposed model is implemented in an incremental and iterative fashion, achieving both local and global convergence. The iteration on the local level involves internal model variables and is performed using the Newton iterative method. Global convergence is attained through a Newton iterative solver as well. The mechanical model is implemented in the FEAP (Finite Element Analysis Program) [42]. The stress tensor computations and the computation of fictitious forces are carried out in MATLAB at the end of each increment after extracting the stress resultants from the FEAP model. The exchange of data is facilitated by MATFEAP [43], a framework extension for FEAP computations. To show the capabilities of the proposed model, we conduct several numerical simulations. Initially, a linear elastic analysis is performed to establish the stress tensor in a shear-dominated example. Subsequently, more computations involving failure under the influence of both tensile and compressive load cases, where the material failure is followed by a global softening response, are presented.

In Section 2, we present the formulations of the proposed model. Numerical simulations are provided in Section 3, while the Discussion and Conclusion are given in Sections 4 and 5, respectively.

2. Novel Discrete Lattice Element Model

The discrete lattice element model proposed in this work is based on the foundation of various existing lattice models commonly employed for the representation of material failure in engineering, particularly in concrete and rocks. Discrete lattice models generally use one-dimensional lattice elements to transmit forces between material particles or distinct portions of the material (grains), which is efficient in simulations of crack and fracture growth. The lattice element models can be represented by truss bars, Euler–Bernoulli beams, or Timoshenko beams [1], or, alternatively, the models may use springs, giving rise to a rigid-body spring model [2]. The unstructured lattice configuration possesses structural randomness, resulting in efficiency in capturing cracks and fractures, which is very beneficial in simulations of failure at lower scales. However, their response at macroscale causes a non-uniform response in the elastic regime, which may significantly reduce their efficiency in capturing crack initiation, especially in case of macroscopic homogenized models.

In the model presented here, we employ a discretization approach based on the Delaunay triangulation of the domain. The Delaunay triangulation is a dual form of Voronoi tessellation, where Voronoi cells represent material particles, such as grains or portions of the material. The Delaunay edges within the triangulation serve as lattice elements, symbolizing cohesive links between Voronoi cells (Figure 1). This structural arrangement enables the representation of cracks through the progressive failure of adjacent lattice elements, providing a comprehensive framework for simulating the complex failure mechanisms observed in concrete and rock materials [1]. In our previous studies, we effectively employed enhanced Timoshenko beams as lattice elements equipped with embedded strong discontinuities to simulate failure in concrete and rocks [13,14,32–36]. In the present study, instead of standard straight Timoshenko beam elements, we employ generalized beam lattice elements based on the kinematics of rigid-body spring models, ensuring the proper elastic displacements and deformations of the discrete model. Previous findings demonstrated the capacity of such discrete models to achieve a correct elastic response [8]. On the other hand, lattice models employing standard beam elements are unable to produce homogeneous strain and stress fields even when Poisson's ratio is equal to zero, although in certain cases an improved response can be achieved if the element parameters are extracted directly from the Voronoi diagram [10,14]. In our generalized beam element model, we introduce the embedded strong discontinuity to ensure captureof the fracture behavior, leading to a new lattice model based on generalized beam elements with embedded discontinuities.

Given that in our work the nodes are placed along the edges of the designated domain and Voronoi cells intersect the boundaries, we employ a mirroring technique to obtain complete cells. This allows us to extract the comprehensive geometrical characteristics of the elements.

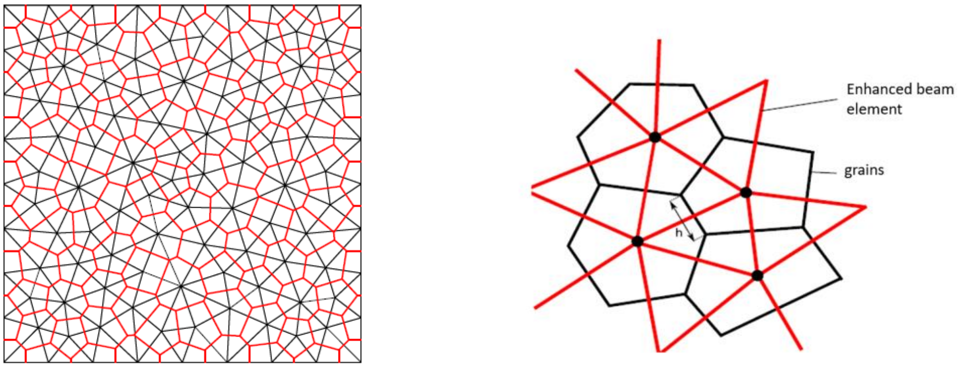

(**a**) (**b**)

Figure 1. (**a**) Structure of discrete lattice model with Voronoi cells as particles of material and lattice elements. (**b**) The proposed enhanced beam element connecting neighboring Voronoi cells. Parameter *h* is extracted from the Voronoi diagram and represents the height of the beam cross section.

2.1. Kinematics of Mechanical Lattice Elements

The formulation of our generalized beam lattice elements is based on the kinematics of rigid-body spring models, where rigid material particles, usually obtained by Voronoi tessellations, are connected by links, as shown in Figure 2. In the rigid-body spring model, each link may be viewed as comprising discrete springs positioned at the midpoint of the edge shared by two adjacent Voronoi cells (point P in Figure 2), representing interacting rigid particles, and two rigid links joined by these springs (segments 1-P and 2-P in Figure 2). The generalized beam lattice element is defined by nodes 1 and 2 and its local coordinate frame x-y. The stiffness of the rigid-body spring in Figure 2 is expressed using elastic constants rather than spring constants. This choice is made to ensure the equivalence of the models.

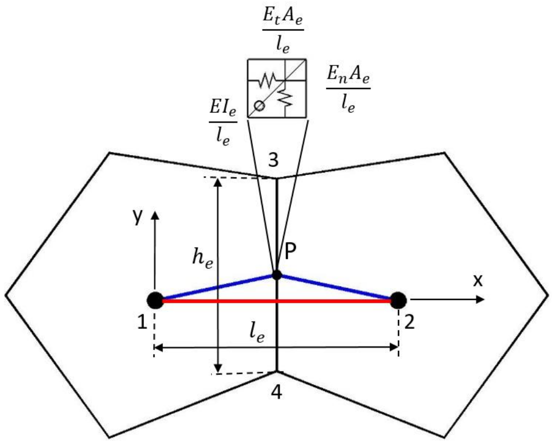

Figure 2. Discrete lattice element model composed of two rigid particles 1 and 2 linked with generalized beam element (red) or rigid-body spring (blue).

Given the displacement and rotation of the particle $I = 1, 2$, $\boldsymbol{u}_I = \begin{bmatrix} u_I & v_I & \theta_I \end{bmatrix}^T$, the displacement at an arbitrary point (x,y) of each particle I is given as

$$\begin{gathered} u = u_I - (y - y_I)\theta_I, \\ v = v_I + (x - x_I)\theta_I, I = 1,\ 2 \end{gathered} \tag{1}$$

The nodal displacement vectors associated with particles $\boldsymbol{u}_I$ are defined with respect to the local coordinate axes of the lattice element, shown in Figure 2, whereby nodes are usually placed at the nuclei of the Voronoi diagram [10,11]. For each generalized beam element, generalized strains $\boldsymbol{\epsilon} = \begin{bmatrix} \epsilon & \gamma & \kappa \end{bmatrix}^T$ may be defined in the local coordinate system

(Figure 2), with ϵ, γ, and κ corresponding to the normal strain, transversal shear strain, and beam curvature, respectively. They can be computed from the vector of element nodal displacements $\mathbf{u} = \begin{bmatrix} u_1 & v_1 & \theta_1 & u_2 & v_2 & \theta_2 \end{bmatrix}^T$ as

$$\boldsymbol{\epsilon} = \mathbf{B}\mathbf{u}, \tag{2}$$

where matrix $\boldsymbol{B}$ represents the strain-displacement matrix in the local coordinate form

$$\boldsymbol{B} = \frac{1}{l_e}\begin{bmatrix} -1 & 0 & y_p & 1 & 0 & -y_p \\ 0 & -1 & -l_e/2 & 0 & 1 & -l_e/2 \\ 0 & 0 & -1 & 0 & 0 & 1 \end{bmatrix}. \tag{3}$$

The generalized beam lattice element represents an extension of the linear Timoshenko beam element used in discrete lattice models [32–36]. A closer inspection and comparison with the corresponding expressions obtained for a linear Timoshenko beam element shows that the curvatures of these two elements are identical, while the shear strain is equal to the value computed at the sample point of a Timoshenko element with selective reduced integration (the Gaussian point positioned at the middle of the element). The only significant difference is encountered in the normal strains (see non-zero terms y_p), arising because here the normal strain is associated with the normal spring force acting at point P, which is in a general case shifted from the straight line connecting nodes by y_p (see Figure 2). Consequently, these two elements possess different stiffness matrices, which become identical only when point P aligns with the local coordinate axis x, as shown in [10].

Motivated by these similarities, in the following, we depart from the kinematics of the rigid-body spring model and consider the links between two adjacent nodes (particles) as a generalized beam model, whose kinematics is defined by Equations (2) and (3). The parameters of these beam lattice elements are computed by extracting certain geometrical properties from the Voronoi network. Namely, each element has its length l_e and cross section area $A_e = h_e \cdot 1$ (1 being the third dimension normal to the model plane, corresponding to unit thickness). Each cross-section height h_e is obtained directly from the Voronoi network from the coordinates of points 3 and 4 (Figure 2). The point P is geometrically placed in the middle of the Voronoi edge perpendicular to the element. The generalized beam lattice element with 3 degrees of freedom per node is shown in Figure 3. The generalized element stress vector is defined in a manner standard in Timoshenko beam models as $\boldsymbol{\sigma} = \begin{bmatrix} N & T & M \end{bmatrix}^T$ and is obtained from generalized strains as

$$\boldsymbol{\sigma} = \mathbf{D}\boldsymbol{\epsilon}, \tag{4}$$

where matrix $\mathbf{D}$ is the diagonal stiffness matrix $\mathbf{D} = \mathrm{diag}(E_n A_e, E_t A_e, EI)$ with moment of inertia $I = 1 \cdot h_e^3/12$. E_n, E_t, and E represent element elastic constants. In this study, in the initial model setups, we set $E_n = E_t = E$, where E corresponds directly to the global modulus of elasticity. Such a setup is equivalent to a global material response with Poisson ratio equal to zero.

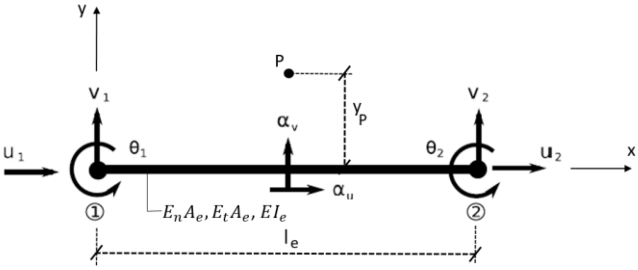

Figure 3. Generalized beam element.

2.2. Stress Tensor Computation and Fictitious Forces

2.2.1. Stress Tensor Computation

The procedure for correcting the model linear elastic response is based on nodal stresses, as proposed in [8]. The nodal stress state is computed from the equilibrium of each particle/node. In order to obtain the stress tensor, we will consider (1) local coordinate systems of each beam element giving rise to longitudinal and transversal forces (Figure 4a) and (2) a virtual cut of each cell (Figure 4b). The longitudinal and transversal element forces N and T of all M lattice elements related to the observed node are considered in the stress tensor computation (Figure 4a).

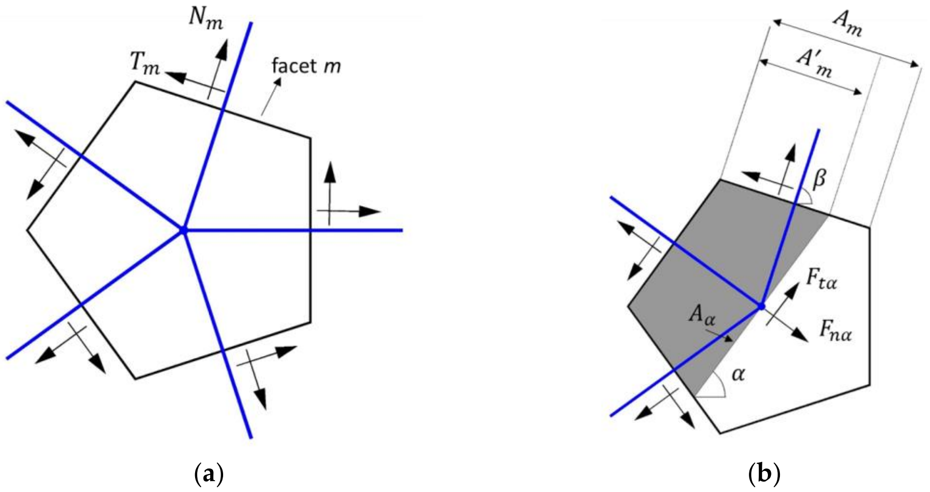

Figure 4. (**a**) Longitudinal and transversal lattice element forces contributing to stress computation; (**b**) total stress resultant vector acting in the section defined by α.

The total stress resultant vector acting in the section defined by α is computed by considering all M elements related to the node as

$$\begin{aligned} F_{n\alpha} &= \sum_{m=1}^{M} w\,[N_m \sin(\beta-\alpha) + T_m \cos(\beta-\alpha)] \\ F_{t\alpha} &= \sum_{m=1}^{M} w\,[N_m \cos(\beta-\alpha) - T_m \sin(\beta-\alpha)], \end{aligned} \tag{5}$$

where the contribution of the stress resultant from every lattice element is multiplied by a weight defined by the ratio $w = A'_m/A_m$ (Figure 4b). The stress components on the section A_α can be computed as

$$\begin{aligned} \sigma_{n\alpha} &= F_{n\alpha}/A_\alpha \\ \sigma_{t\alpha} &= F_{t\alpha}/A_\alpha, \end{aligned} \tag{6}$$

The stress tensor can be defined by computing the components in two perpendicular sections obtained by positioning the section with $\alpha = 0°$ (Figure 5a) and $\alpha = 90°$ (Figure 5b).

By taking the total stress resultant vector on the cut planes, we can compute the stress components $\sigma_{XX} = F_{n\alpha}/A_\alpha$ and $\tau_{XY} = F_{t\alpha}/A_\alpha$ for $\alpha = 90°$; $\tau_{YX} = F_{t\alpha}/A_\alpha$ and $\sigma_{YY} = F_{n\alpha}/A_\alpha$ for $\alpha = 0°$. The corresponding nodal stress tensor is symmetric since $\tau_{XY} = \tau_{YX}$

$$\sigma = \begin{bmatrix} \sigma_{XX} & \tau_{XY} \\ \tau_{YX} & \sigma_{YY} \end{bmatrix} \tag{7}$$

where X and Y refer to the global coordinate axes.

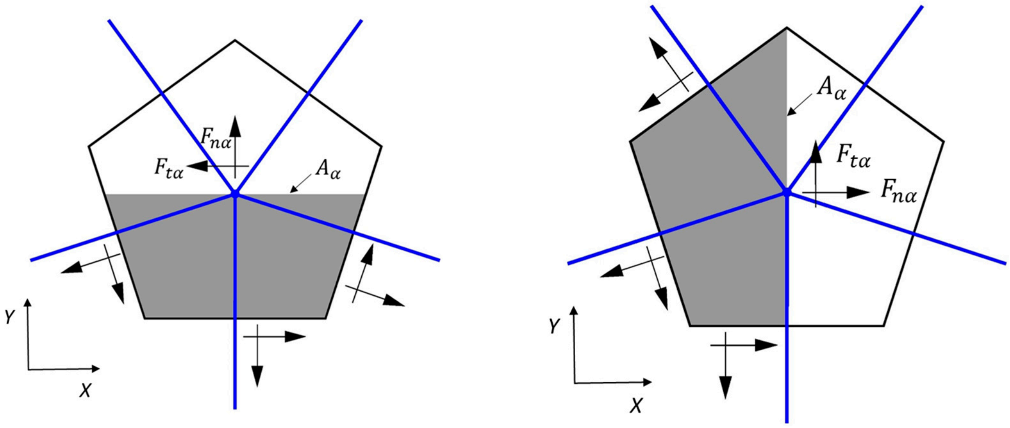

(**a**) (**b**)

Figure 5. Two perpendicular cut planes for retrieving the stresses. (**a**) Cut plane $A_{\alpha=0}$, (**b**) cut plane $A_{\alpha=90}$.

2.2.2. Fictitious Forces

Fictitious forces are utilized to adjust the elastic model response for various Poisson ratio values. These forces are introduced into the model as an additional load that must be incorporated into the residual force vector. Firstly, the principal stresses σ_1 and σ_2 are computed for an initial state of $\nu = 0$, along with the corresponding principal deformations ε_1 and ε_2. Fictitious deformations are further computed by using these principal strains and the required Poisson ratio, as presented in [8]:

$$\begin{aligned} \varepsilon_1^{fic} &= \nu\varepsilon_2 \\ \varepsilon_2^{fic} &= \nu\varepsilon_1. \end{aligned} \tag{8}$$

By multiplying by the modulus of elasticity E, we can compute the fictitious stresses:

$$\begin{aligned} \sigma_1^{fic} &= E\varepsilon_1^{fic} \\ \sigma_2^{fic} &= E\varepsilon_2^{fic}. \end{aligned} \tag{9}$$

The corresponding nodal fictitious forces (Figure 6a) can be computed as:

$$F_1^{fic} = \sigma_1^{fic} A_{\alpha,1},\ F_2^{fic} = \sigma_2^{fic} A_{\alpha,2}, \tag{10}$$

where areas $A_{\alpha,1}$ and $A_{\alpha,2}$ correspond to the principal stress planes.

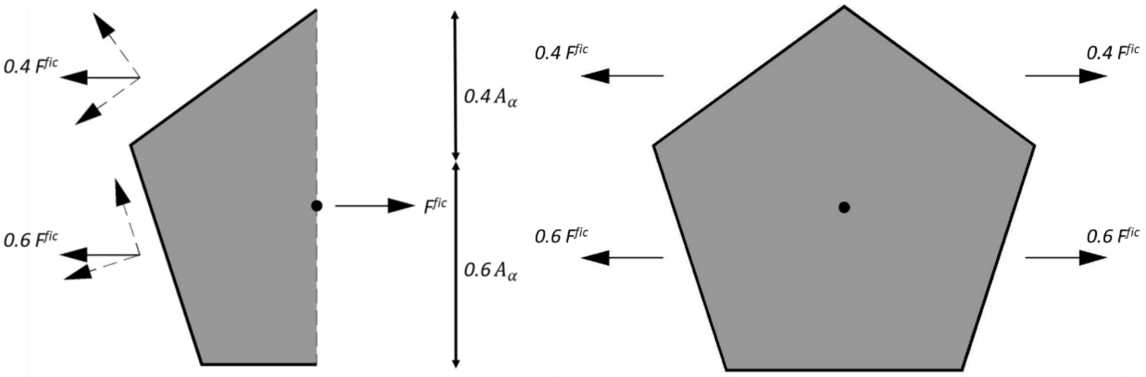

(**a**) (**b**)

Figure 6. (**a**) The cut plane through the Voronoi cell for computation of nodal fictitious force. (**b**) The distribution of nodal fictitious forces on a cell.

The nodal fictitious force is in equilibrium with the forces acting in the neighboring elements of the Voronoi cell (Figure 6b). Each elemental force is proportional to the projected area of the Voronoi cell on the cut plane $A_{\alpha,1}$. After the elemental forces are computed, they are projected into the local coordinate system of the elements and added to the corresponding lattice elements.

The algorithm for the computation of fictitious forces relies on an iterative procedure for general stress states. However, in the simple cases considered in this paper, iterations are not required [8].

2.3. Failure Mechanics

The failure mechanism of a lattice element is controlled through the incorporation of an embedded strong discontinuity [17,18]. The discontinuity is placed in the middle of the generalized lattice beam finite element, corresponding to the position of the Gauss integration point and the location of the crack between the Voronoi cells. This involves introducing a jump in the displacement field along both the longitudinal and transversal directions of the element, achieved by applying a Heaviside function [32–36]. The formulation of the lattice element is expressed in the fashion of the finite element method, utilizing linear interpolation functions. This finite element formulation is implemented in the FEAP finite element code.

The model is capable of representing both Mode I and Mode II failure mechanisms by introducing embedded discontinuities along both the longitudinal and transversal directions of the element. The Heaviside function is defined as $H_{x_p} = 0$ for $x \leq x_p$ and $H_{x_p} = 1$ for $x > x_c$. The vector $\boldsymbol{\alpha} = \begin{bmatrix} \alpha_u & \alpha_v & 0 \end{bmatrix}^T$ represents the jump in the displacement field at the position of discontinuity (in the middle of the element), as shown in Figure 3. The enhanced displacement field can be written as the sum of the regular and discontinuous (singular) part:

$$\mathbf{u}(x) = \overline{\mathbf{u}}(x) + \boldsymbol{\alpha} H_{x_p} = \begin{bmatrix} \overline{u}(x) \\ \overline{v}(x) \\ \overline{\theta}(x) \end{bmatrix} + \begin{bmatrix} \alpha_u \\ \alpha_u \\ 0 \end{bmatrix} H_{x_c}, \tag{11}$$

The displacement field can be written in the fashion of finite element interpolations:

$$\mathbf{u}(x) = N_1(x)\mathbf{u}_1 + N_2(x)\mathbf{u}_2 + \boldsymbol{\alpha}\underbrace{(H_{x_c} - N_2(x))}_{M(x)}, \tag{12}$$

where the regular part is interpolated with the linear shape functions $N_1(x) = 1 - \frac{x}{l_e}$, $N_2(x) = \frac{x}{l_e}$ and $(H_{x_c} - N_2(x))$ represents the interpolation function $M(x)$ in the fashion of the embedded strong discontinuity:

$$M(x) = \begin{cases} -\frac{x}{l_e}; x \in [0,\ x_c\rangle \\ 1 - \frac{x}{l_e};\ x \in \langle x_c,\ l_e] \end{cases}. \tag{13}$$

The discontinuity parameters $\boldsymbol{\alpha}$ are computed locally. The enhanced displacement field can be written in matrix form as:

$$\mathbf{u} = \mathbf{N}\mathbf{u} + \mathbf{M}\boldsymbol{\alpha}, \tag{14}$$

where $\mathbf{N}$ represents the matrix of interpolation functions $N_1(x)$ and $N_2(x)$ with the dimension 3×6, while the 3×3 matrix $\mathbf{M} = \mathrm{diag}[\mathrm{M(x)}, \mathrm{M(x)}, 0]$ contains $M(x)$ discontinuity functions. The enhanced deformation field can be written as the sum of regular $\overline{\boldsymbol{\epsilon}}(x)$ and singular part $\boldsymbol{\alpha}\delta_{x_c}$

$$\boldsymbol{\epsilon}(x) = \overline{\boldsymbol{\epsilon}}(x) + \boldsymbol{\alpha}\delta_{x_c} = \begin{bmatrix} \overline{\epsilon}(x) \\ \overline{\gamma}(x) \\ \overline{\kappa}(x) \end{bmatrix} + \begin{bmatrix} \alpha_u \\ \alpha_v \\ 0 \end{bmatrix} \delta_{x_c}. \tag{15}$$

The Dirac function δ_{x_c} tends to infinity for $x = x_c$; otherwise, it is zero. The matrix form of the deformation field can be written as

$$\boldsymbol{\epsilon} = \mathbf{B}\mathbf{u} + \overline{\mathbf{G}}\boldsymbol{\alpha} + \boldsymbol{\alpha}\delta_{x_c}, \tag{16}$$

where matrix **B** is a strain-displacement matrix from (2) and (3) written in finite element interpolation form containing the shape functions $N_1(x)$ and $N_2(x)$ and their derivatives $B_1(x)$ and $B_2(x)$, and $\overline{\mathbf{G}} = \mathrm{diag}\left[\overline{\mathrm{G}}(\mathrm{x}), \overline{\mathrm{G}}(\mathrm{x}), 0\right]$ contains

$$\overline{G}(x) = -\frac{1}{l_e}. \tag{17}$$

In order to construct the virtual work, the virtual deformation field can be constructed as

$$\delta\boldsymbol{\epsilon} = \mathbf{B}\delta\mathbf{u} + \overline{\mathbf{G}}\delta\boldsymbol{\alpha} + \delta\boldsymbol{\alpha}\delta_{x_c}, \tag{18}$$

where $\delta\boldsymbol{\epsilon}$, $\delta\mathbf{u}$**,** and $\delta\boldsymbol{\alpha}$ represent the virtual counterparts of strain, displacement, and virtual discontinuity jumps, respectively. The virtual work equation can be expressed as the contribution of internal and external virtual work

$$G^{int,(e)} - G^{ext,(e)} = 0. \tag{19}$$

The virtual work equation produces the internal force vector equation and the local residual equation due to discontinuity:

$$\begin{gathered} \mathbf{f}^{int,(e)} = \int_0^{l_e} \mathbf{B}^T \boldsymbol{\sigma} dx, \\ \mathbf{h}^{(e)} = \int_0^{l_e} \left(\overline{\mathbf{G}} + \delta_{x_c}\right) \boldsymbol{\sigma} dx = \int_0^{l_e} \overline{\mathbf{G}} \boldsymbol{\sigma} dx + \mathbf{t} \end{gathered} \tag{20}$$

From the condition that the local residual needs to be enforced to zero, we obtain the expression for the traction vector at the discontinuity

$$\mathbf{t} = -\int_0^{l_e} \overline{\mathbf{G}} \boldsymbol{\sigma} dx. \tag{21}$$

2.4. Damage Constitutive Law for Softening

The description of energy dissipation in the material involves the softening damage law, which relates traction in the discontinuity with the jump in the displacement field. When the stress in the material surpasses the ultimate strength of the specified material, a discontinuity occurs, accompanied by the activation of a jump in the displacement field. As the jump in displacement field increases, indicative of crack opening, the load-bearing capacity decreases, leading to a reduction in stress at the discontinuity and a consequent decrease in material stiffness. Material unloading results in crack unloading, but the accumulated material damage and reduced stiffness persist. Complete unloading causes the crack to close, and the displacement field jump becomes zero. Upon reloading, it depends on the reduced material stiffness, following the inverse value of the softening modulus (Figure 7).

The damage model is formulated in the thermodynamics framework and free energy ψ:

$$\psi\left(\overset{=}{\overline{D}}, \alpha, \overset{=}{\overline{\xi}}\right) = \frac{1}{2}\overset{=}{\overline{D}}^{-1} \alpha^2 + \Xi\left(\overline{\xi}\right), \tag{22}$$

where $\overset{=}{\overline{D}}$ and α represent the damage compliance modulus and the displacement jump, respectively. The softening variable is defined as $\Xi(\xi) = -\overset{=}{\overline{q}}\,\overset{=}{\overline{\xi}}$. The failure detection function $\overset{=}{\overline{\phi}}$ can be defined as:

$$\overline{\overline{\phi}}\left(t,\overline{\overline{q}}\right) = |t| - \left(\sigma_u - \overline{\overline{q}}\right), \tag{23}$$

where t represents the traction vector at the discontinuity, σ_u is the ultimate stress level, and $\overline{\overline{q}}$ represents the softening function, defined as:

$$\overline{\overline{q}} = \sigma_u\left(1 - exp\left(-\overline{\overline{\xi}}\frac{\sigma_u}{G_f}\right)\right). \tag{24}$$

G_f represents the fracture energy. The expression for the traction vector at the discontinuity can be obtained as

$$t = \frac{\partial\psi}{\partial\alpha} = \overline{\overline{D}}^{-1}\alpha,\ \overline{\overline{D}} \in [0,\infty\rangle. \tag{25}$$

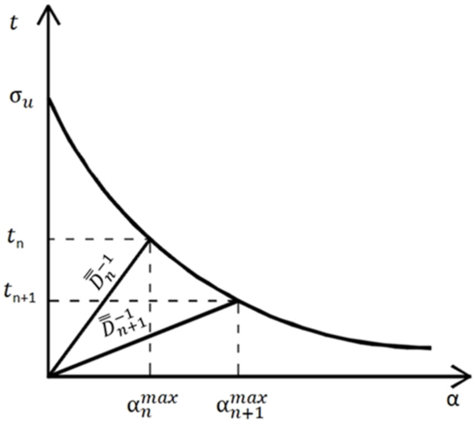

Figure 7. The damage constitutive law.

2.5. Fracture Criteria

The proposed model adopts a discrete representation of fracture, with the crack orientation perpendicular to the lattice element, aligning with the Voronoi cells. In this framework, the lattice element is allowed to undergo failure in both Mode I, representing tensile opening, and Mode II, representing shear sliding. Additionally, the model can simulate mixed-mode failure, where both criteria are simultaneously activated. The failure criteria are based on the maximum tensile stress and maximum shear stress permitted within the lattice element. This approach allows for a comprehensive simulation of various fracture mechanisms occurring under different loading conditions. The failure functions for both modes are written in the framework of damage mechanics and obtained as expression (23), while being applied to traction vectors in both directions:

$$\begin{aligned} \overline{\overline{\phi}}\left(t_u,\overline{\overline{q}}_u\right) &= t_u - \left(\sigma_u - \overline{\overline{q}}_u\right) \\ \overline{\overline{\phi}}\left(t_v,\overline{\overline{q}}_v\right) &= |t_v| - \left(\tau_u - \overline{\overline{q}}_v\right). \end{aligned} \tag{26}$$

The failure criteria are localized within individual lattice elements, determined by the local stresses. This approach enables the activation of numerous local cracks and fractures within the lattice structure. However, the model allows for the occurrence of multiple local cracks that subsequently merge and coalesce. This process leads to the formation of new, large-scale fractures through the mechanism of internal force redistribution. Through such interactions, the model captures the global fracture mechanisms resulting from the merging of smaller-scale cracks, providing a representation of the material response to varying loading conditions.

2.6. Exchange of Data between FEAP and MATLAB

The proposed mechanical model is implemented in the Finite Element Analysis Program (FEAP) [42]. Nevertheless, the computation of the stress tensor in nodes and the calculation of fictitious forces take place in MATLAB. To ensure data exchange between FEAP and MATLAB, we employ the MATFEAP interface [43]. The lattice element forces in the local element frame are first extracted from FEAP. Once the fictitious forces are computed on the basis of the extracted values of forces in MATLAB, they are then transferred to FEAP via the interface and incorporated into the internal force vector. This integrated approach allows for consistent and effective communication between the two platforms, enabling the final computation of displacements within the FEAP environment. The exchange of data between the two platforms is performed in each time step. However, when the first fractures are initiated, the algorithm for the computation of fictitious forces stops, since the specimen no longer behaves as an elastic continuum, but it changes to a discrete and discontinuous state.

3. Numerical Simulations

In this work, we conduct several numerical simulations to present the capabilities of the proposed discrete lattice element model with improved elastic response. While discrete lattice models are commonly applied in mesoscale simulations of failure with heterogeneous structures, our simulations involve specimens composed of a single material, designed to first exhibit elastic continuum behavior prior to the appearance of fractures. At each increment of the simulation, the fracture initiation criteria are examined for all lattice elements. Once the initial fractures start to propagate, the specimen undergoes a transition from a continuum material to a fractured state, while at the same time, the algorithm for fictitious forces ensuring continuum-like behavior in the lattice model stops. Quasi-static propagation of fractures is considered here, although fast dynamic simulation can be conducted by adding inertia terms to the discrete lattice model [14].

The presented damage softening model is suitable for brittle and quasi-brittle failure of engineering materials, usually observed in composite materials and structures [14]. The ductile failure can alternatively be conducted with a plasticity-based softening model [13]. The distinction between these two models is in using internal thermodynamics variables. Although the focus here relies on quasi-brittle failure with a damage softening model, a plasticity-based model can be implemented with the proposed enhanced discrete lattice model.

To illustrate the model performance, we initiate the simulation with a test where shear stresses dominate. In this example, only stress computations are carried out and compared with those from a standard continuum element model. Subsequently, monotonic uniaxial tension and compression tests are conducted until failure, where the model is providing the continuum-like behavior prior to the initiation of cracks. Post-fracture initiation, the model allows for the further propagation of tensile and shear cracks by activating the formulation of embedded strong discontinuities. The proposed model simulates monotonic load increase until failure, but it can also simulate unloading. Indeed, an unloading mechanism is present in a significant number of elements that initiated cracks but did not suffer significant damage. Moreover, it is also possible to build a model that can capture cyclic loading conditions on the basis of the proposed kinematics.

The implementation of the model is carried out in both FEAP and MATLAB, with the MATFEAP interface facilitating the exchange of data between the two codes, as elaborated in the preceding section.

In all simulations, the domain is discretized using the Delaunay algorithm, and this process is accomplished through the utilization of GMSH [44]. The discrete lattice elements are then extracted from the resulting mesh. Concurrently, the geometric properties and characteristics pertaining to the Voronoi network are also obtained from the discretized domain. In our work, we employ rectangular domains. The utilization of more complex geometries involving potential inclusions and multi-phase materials would necessitate an iterative procedure in the computation of fictitious forces. This is due to the more complex stress states inherent in such configurations, leading to increased computational requirements.

3.1. Shear-Dominated Example

In the shear-dominated test, a load inducing shear stresses is applied to a rectangular domain, as depicted in Figure 8. More precisely, horizontal displacement is imposed on the top of the specimen. This test is performed using the proposed discrete lattice model with a Poisson ratio set to zero. To capture the stresses in this test, the methodology outlined in Section 2.2.1 is followed. The proposed model is designed to accurately represent the response of a linear elastic continuum when the Poisson ratio is zero, similar to the rigid-body spring model presented in [8]. The mechanical and geometrical characteristics of the test are detailed in Table 1. The discrete lattice model consists of 4842 lattice elements. Figure 9a illustrates the computed nodal stress component, specifically focusing on shear stress. The computed nodal stress obtained using the discrete lattice model is then compared to the results from a standard FEAP solid-element model (Figure 9b) with identical characteristics. The stress values obtained from these two cases align, showing the accuracy and reliability of the proposed discrete lattice model in capturing the shear-dominated response.

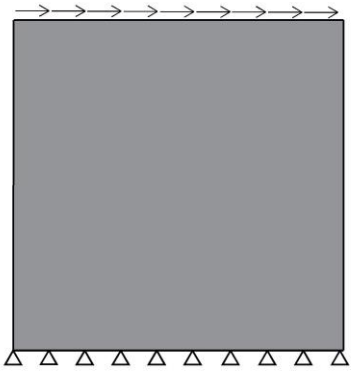

Figure 8. Shear test with boundary conditions.

Table 1. The mechanical characteristics and geometry of the specimen for shear test.

Shear Test
$E = 10$ GPa, $\nu = 0$ Specimen dimensions $100 \times 100 \times 1$ cm

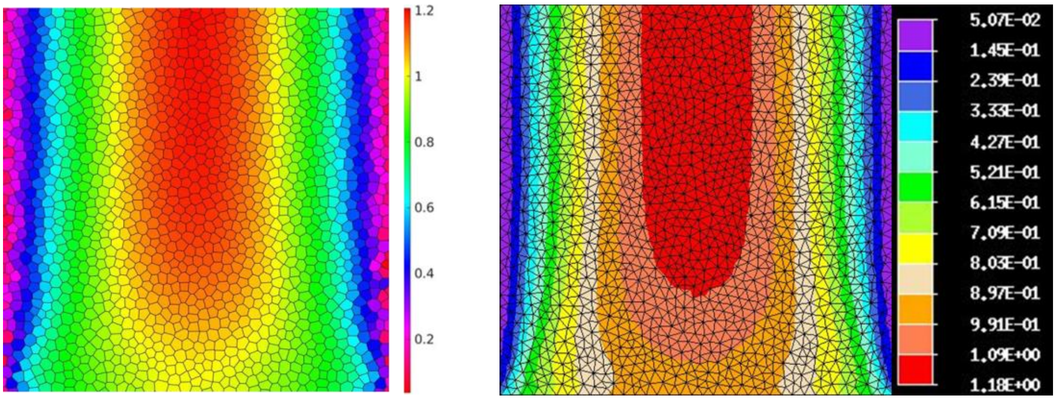

(**a**) (**b**)

Figure 9. Comparison of shear stress state for: (**a**) discrete lattice model; (**b**) FEAP linear solid element (CST).

3.2. Uniaxial Tension Test

Uniaxial tension tests were conducted on specimens with identical geometric and mechanical characteristics (Table 2), employing two different meshes, as illustrated in Figure 10. Symmetrical constraints were applied to the bottom edge of the specimen, as depicted in Figure 10, to ensure a symmetric response in terms of deformations in the lateral direction. The test involved applying an imposed displacement on the top edge of the specimen. The primary objective of this test was to examine the discrete model's capacity to accurately simulate local deformations in the elastic regime and post-peak softening behavior.

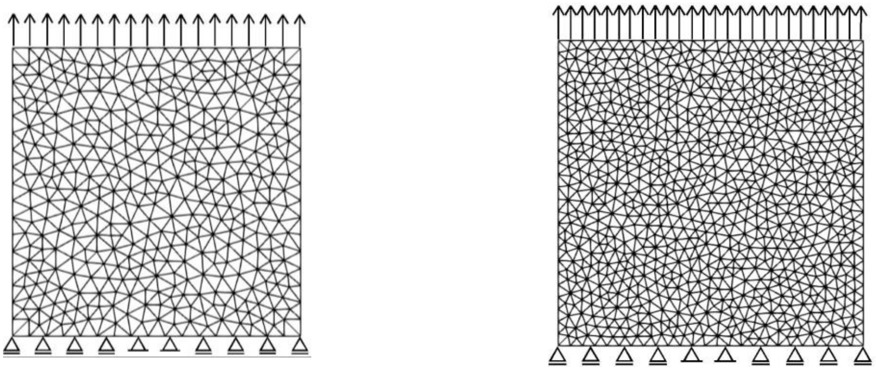

(**a**) (**b**)

Figure 10. Uniaxial tension test meshes: (**a**) Mesh1-1210; (**b**) Mesh2-2570.

Table 2. The mechanical characteristics and geometry of the specimen.

Uniaxial Tension and Compression Test
$E = 10$ GPa, $\nu = 0.2$
$\sigma_{u,c} = 12$ MPa, $\sigma_{u,t} = 2\ MPa$, $\tau_u = 2.5$ MPa
$G_{f,I}^{(c)} = 200$ N/m, $G_{f,I}^{(t)} = 2$ N/m, $G_{f,II} = 30$ N/m
Dimensions of the specimen 10 × 10 × 1 cm

Simulations are conducted using imposed displacement control. Figure 11 presents the complete macroscopic reaction–displacement curve, where the specimen initially behaves like a linear elastic continuum. Subsequently, cracks initiate, marking the transition from a continuous to a discontinuous state. The observed drop in the macroscopic curve and subsequent softening signify the progressive degradation of the specimen until it is entirely softened, losing its carrying capacity.

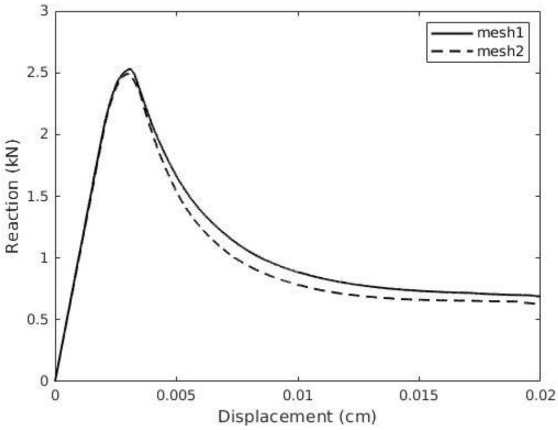

Figure 11. Comparison of results for tension test for two different meshes.

Figure 12 illustrates displacement plots on the discrete lattice network of elements at the imposed displacement level of 0.001 cm. At this stage, the specimen remains in the linear elastic regime, and no cracking has occurred. These plots demonstrate that the proposed algorithm of fictitious forces ensures correct displacements and deformations of the specimen. The lateral displacements correspond to a Poisson ratio of 0.2, as specified in the input parameters of the simulation. The algorithm achieves accurate deformation of the discrete lattice network by computing fictitious forces based on the stress tensor, correctly determining the principal stress in the nodes aligned with the global *y*-axis.

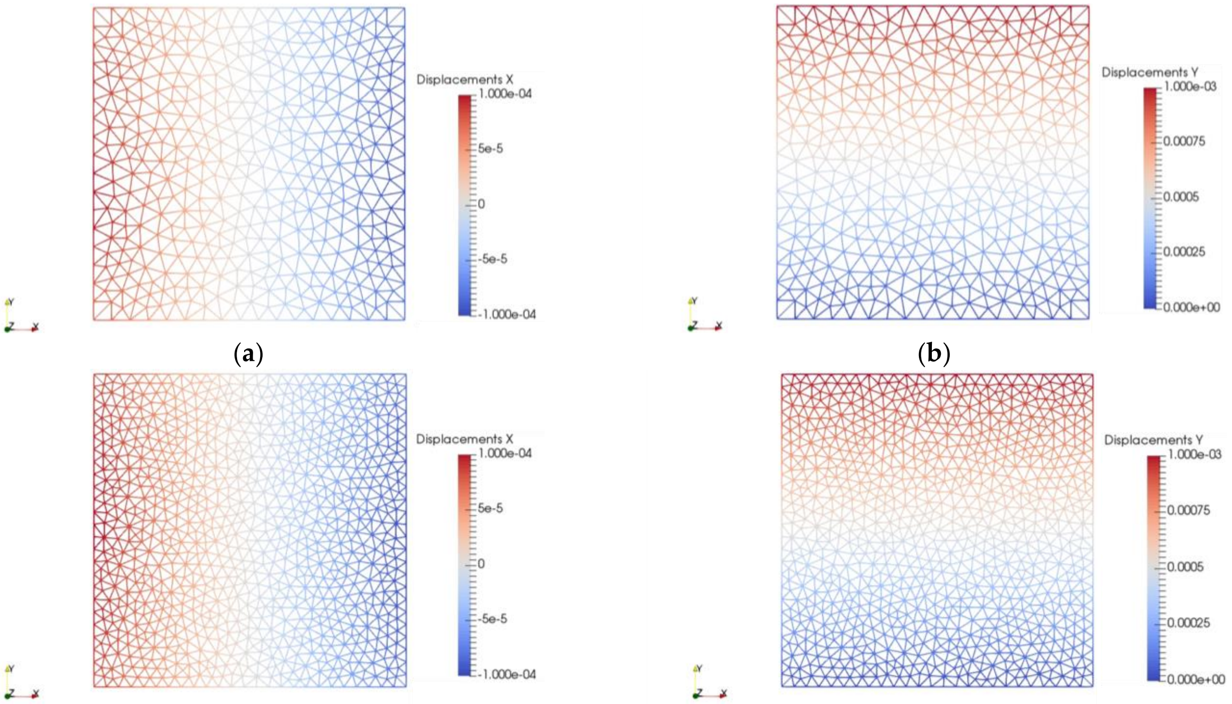

(**a**) (**b**)

(**c**) (**d**)

Figure 12. Displacement of Voronoi nodes for tension test for imposed displacement 0.001 cm for ν = 0.2: (**a**) displacement in direction x-Mesh1; (**b**) displacement in direction y-Mesh1; (**c**) displacement in direction x-Mesh2; (**d**) displacement in direction y-Mesh2.

Uniform results in linear elastic regime deformations are attained for both lattice meshes when the input parameters are defined on the global level. Conversely, failure in the discrete lattice network initiates with the initiation of the first cracks, with the failure criteria and parameters defined on the local element level. The final state of the cracks at the end of the simulation is depicted in Figure 13, where the failed elements are highlighted in red. On a global scale, a dominant macro-crack propagates through the entire domain, extending perpendicular to the imposed displacement direction. However, the cracks leading to total failure exhibit slight variations in length and local directions between the two meshes, even with the use of identical fracture parameters. This discrepancy arises due to the inherent randomness in stiffness within each lattice element, impacting the failure regime. As the failure criteria are applied to each lattice beam element, this internal heterogeneity determines the weakest link, highlighting the effectiveness of the lattice model in terms of robust crack propagation and path determination. Thus, the proposed lattice model effectively simulates deformations related to a continuum response in the linear elastic regime, while the fracture behavior is governed by the internal heterogeneity within the network, rendering it robust in terms of crack propagation. The uniaxial tension test failure mechanism computed with the proposed model aligns well with the phase-field simulation of concrete failure presented in [45], where the crack is perpendicular to the direction of tensile loading, while its morphology corresponds to concrete internal heterogeneities.

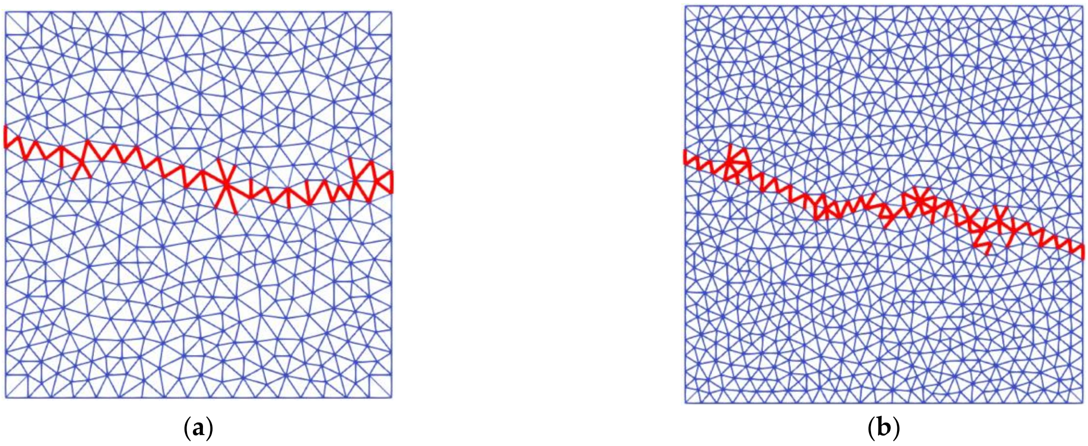
(**a**) (**b**)

Figure 13. Macro-crack at the end of tension test for: (**a**) Mesh1-1210; (**b**) Mesh2-2570.

While the global fractures leading to the specimen's total failure exhibit slight variations due to inherent variability, the overall global responses in terms of softening and dissipated energy remain very close to each other, as depicted in Figure 11. The minimal difference in the global response can be attributed to the length of the cracks. However, this disparity is minor within the softening curves, despite differences in the element sizes between Mesh 1 and Mesh 2. This characteristic represents a significant advantage of the proposed fracturing algorithm and model—the softening behavior is not dependent on the mesh size. Instead, it solely relies on the fracture energy, which is an input parameter. This dependency on fracture energy is a direct consequence of the embedded strong discontinuities, which act as localization limiters for softening. This stands in contrast to models where the softening response may be influenced by variations in mesh size, highlighting the robustness and reliability of the proposed approach.

3.3. Uniaxial Compression Test

In the uniaxial compression test, the specimens possess identical mechanical and geometrical properties, along with the same meshes from the uniaxial tension test. This test shows the discrete lattice model's capability to accurately simulate local deformations in the elastic regime and post-peak softening behavior, but under uniaxial compressive loading conditions. Simulations in the compression test are conducted using imposed displacement control, as illustrated in Figure 14. Figure 15 displays the displacement plot at an imposed displacement level of 0.004 cm, where the specimen remains intact and in the linear elastic regime.

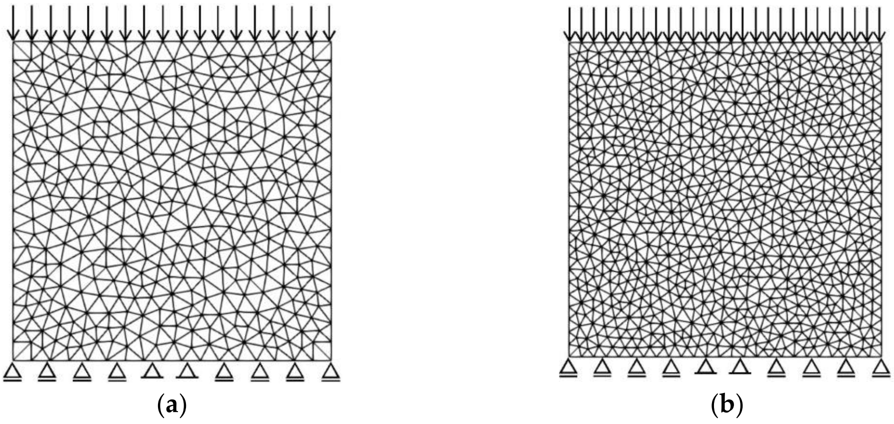
(**a**) (**b**)

Figure 14. Uniaxial compression test meshes: (**a**) Mesh1-1210; (**b**) Mesh2-2570.

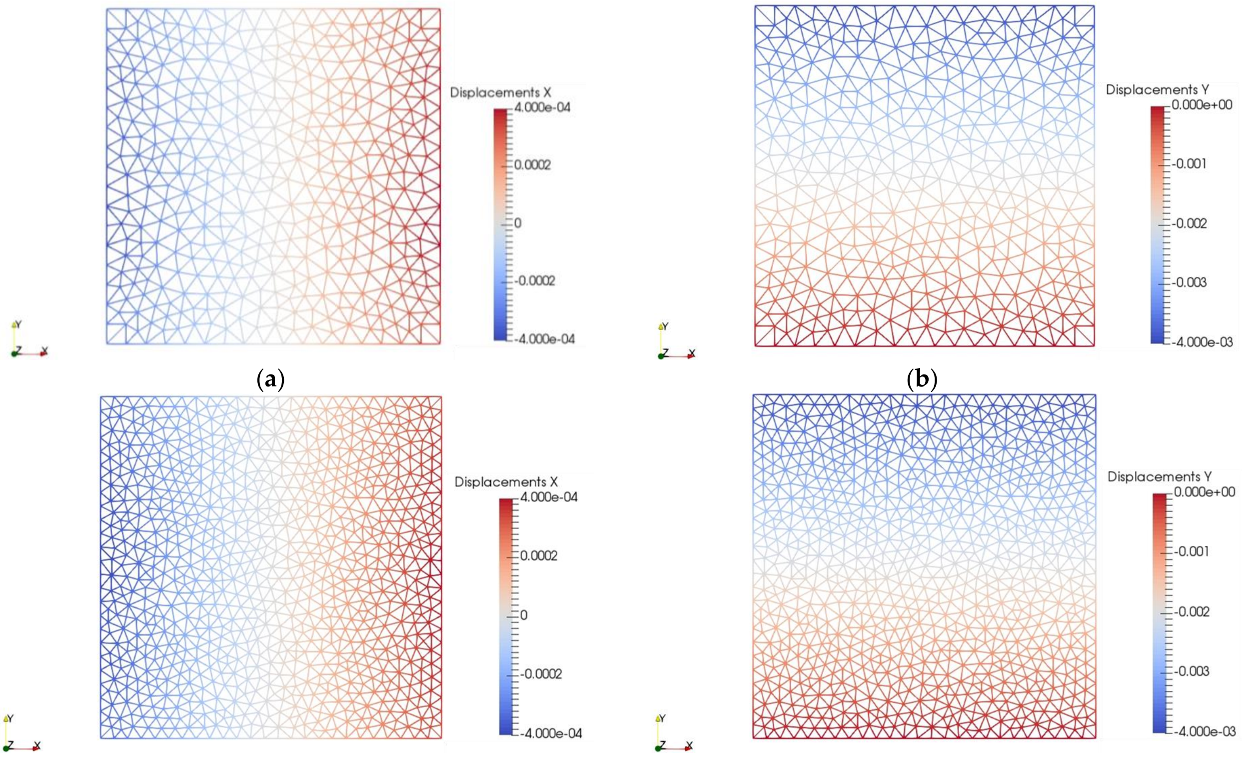

(**a**) (**b**) (**c**) (**d**)

Figure 15. Displacement of Voronoi nodes for compression test for imposed displacement 0.004 cm for $\nu = 0.2$: (**a**) displacement in direction x-Mesh1; (**b**) displacement in direction y-Mesh1; (**c**) displacement in direction x-Mesh2; (**d**) displacement in direction y-Mesh2.

The plots in Figure 15 reveal that the specimen undergoes lateral expansion, and the ratio of horizontal to vertical displacements aligns with the desired Poisson ratio of 0.2. This accurate deformation in the lateral direction is achieved through the application of the fictitious-force approach, as discussed previously. Both meshes respond effectively to the introduced fictitious forces in the internal force vector, ensuring the proper linear elastic response.

However, the initiation of the first fractures causes the specimen to transition into a discontinuous state until total failure. The macroscopic responses in terms of the reaction–displacement curve in Figure 16 illustrate the material softening during the failure process. Slight differences in the amount of total dissipated energy and softening are observed between the two meshes due to a slightly varied failure mechanism arising from internal heterogeneity and the randomness of the lattice network.

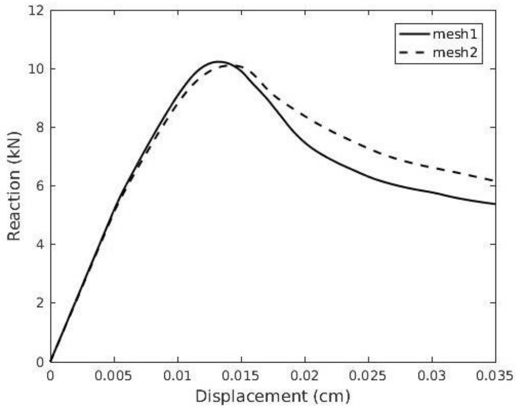

Figure 16. Comparison of results for compression test for two different meshes.

The final failure patterns illustrated in Figure 17 reveal a typical uniaxial compression test failure mechanism, where the dominant macro-crack takes a diagonal form due to shear sliding. The diagonal form of the dominant crack in the uniaxial compression test is typical for quasi-brittle materials such as concrete, as shown in the experiment provided in [45].

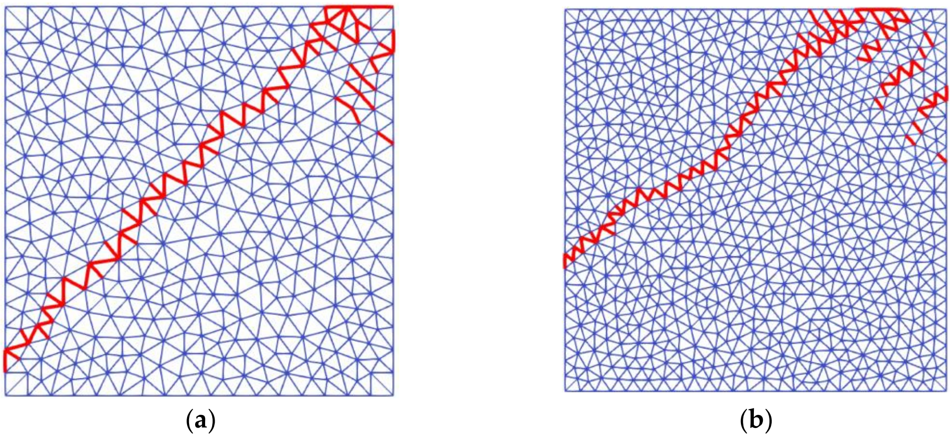

Figure 17. Macro-crack at the end of compression test for: (**a**) Mesh1-1210; (**b**) Mesh2-2570.

Similar failure patterns are observed with both meshes, although the length and angle of the macro-cracks exhibit slight differences due to internal randomness. Despite these variations, the proposed discrete lattice model effectively captures the essential aspects of the uniaxial compression test while being robust in simulating complex fracture behaviors under applied loading conditions.

4. Discussion

The novel discrete lattice element model developed in this study represents a contribution in addressing challenges related to simulating the elastic response and fracture propagation with softening in materials and structures by using discrete lattice models. The model introduces improvements by ensuring that the local elastic lattice parameters correspond to global material elastic constants, allowing for the accurate simulation of various Poisson ratios and easier model characterization. At the same time, the model also successfully achieves mesh-independent post-peak softening responses, which is a nontrivial challenge in discrete lattice models. Here, this has been achieved through the integration of the embedded strong discontinuity framework. Through numerical examples, we demonstrated the model's capability to accurately represent stress tensors in shear-dominated scenarios. Additionally, the model presented the ability to reproduce typical failure mechanisms observed in uniaxial tension and compression tests, such as horizontal tensile cracking and diagonal shear fractures, respectively. The use of two different meshes in these tests revealed consistent macroscopic elastic responses, which is observed in the real-world behavior of engineering materials with inherent heterogeneities. While the global fracture softening responses exhibited close agreement, subtle deviations highlighted the influence of internal material heterogeneities on failure mechanisms, a phenomenon common in real engineering materials. The lattice element model naturally incorporates randomness in the mesh configurations, adding robustness to its ability to simulate various fracture mechanisms.

The proposed discrete lattice element model with an improved elastic response demonstrates robust computational efficiency by using one-dimensional elements. The incorporation of the kinematics from the rigid-body spring model into a generalized beam lattice finite element aligns with computational efficiency as well. The softening based on a damage model [21–23] effectively captures monotonic failure in quasi-brittle and brittle materials. However, it should be noted that the model has limitations in representing cyclic behavior. While the current framework favors a quasi-static regime, neglecting inertial effects and propagation rates [14,34], potential extensions could be explored to incorporate cyclic behavior on the basis of proposed kinematics.

5. Conclusions

The proposed discrete lattice element model not only captures the correct elastic response but also embraces the inherent variability in material behavior, providing a comprehensive representation of the material response from uniform elasticity to fracture mechanisms influenced by internal heterogeneities. This work provides a capable model for simulation and understanding of material behavior in engineering applications.

Author Contributions: Research conduction and programming, J.Č.; software, J.Č. and M.N.; writing, J.Č., E.M., T.J. and M.N.; discrete lattice element mathematical modelling, E.M. and T.J.; conceptualization, M.N.; supervision, M.N.; funding acquisition, M.N.; project management, M.N. All authors have read and agreed to the published version of the manuscript.

Funding: This research was funded by the Croatian Science Foundation project 'Parameter estimation framework for fracture propagation problems under extreme mechanical loads' (HRZZ-UIP-2020-02-6693). The research is partially supported through the project KK.01.1.1.02.0027, co-financed by the Croatian Government and the European Union through the European Regional Development Fund—the Competitiveness and Cohesion Operational Programme. Finally, the partial support through the PID2022-140117NB-I00 Research Project, financed by the European Union from the MCIN/AEI/10.13039/501100011033/"ERDF A way of making Europe", is acknowledged.

Institutional Review Board Statement: Not applicable.

Informed Consent Statement: Not applicable.

Data Availability Statement: The data presented in this study are available on request from the corresponding author. The data are not publicly available due to dependency on our software implementation.

Conflicts of Interest: The authors declare no conflicts of interest.

References

1. Nikolic, M.; Karavelic, E.; Ibrahimbegovic, A.; Miscevic, P. Lattice Element Models and Their Peculiarities. *Arch. Comput. Methods Eng.* **2018**, *25*, 753–784. [CrossRef]
2. Bolander, J.E.; Eliáš, J.; Cusatis, G.; Nagai, K. Discrete mechanical models of concrete fracture. *Eng. Fract. Mech.* **2021**, *257*, 108030. [CrossRef]
3. Munjiza, A.; Bangash, T.; John, N.W.M. The combined finite–discrete element method for structural failure and collapse. *Eng. Fract. Mech.* **2004**, *71*, 469–483. [CrossRef]
4. Schlangen, E.; Van Mier, J.G.M. Simple lattice model for numerical simulation of fracture of concrete materials and structures. *Mater. Struct.* **1992**, *25*, 534–542. [CrossRef]
5. Cusatis, G.; Bažant, Z.P.; Cedolin, L. Confinement-shear lattice CSL model for fracture propagation in concrete. *Comput. Method. Appl. Mech.* **2006**, *25*, 7154–7171. [CrossRef]
6. Zhang, H.; Savija, B.; Figueiredo, S.C.; Schlangen, E. Experimentally validated multi-scale modelling scheme of deformation and fracture of cement paste. *Cem. Concr. Res.* **2017**, *102*, 175–186. [CrossRef]
7. Chao, J.; Zhao, G.F.; Nasser, K. On crack propagation in brittle material using the distinct lattice spring model. *Int. J. Solids Struct.* **2017**, *118–119*, 41–57.
8. Asahina, D.; Ito, K.; Houseworth, J.E.; Birkholzer, J.T.; Bolander, J.E. Simulating the Poisson effect in lattice models of elastic continua. *Comput. Geotech.* **2015**, *70*, 60–67. [CrossRef]
9. Asahina, D.; Aoyagi, K.; Kim, K.; Birkholzer, J.T.; Bolander, J.E. Elastically-homogeneous lattice models of damage in geomaterials. *Comput. Geotech.* **2017**, *81*, 195–206. [CrossRef]
10. Bolander, J.E.; Saito, S. Fracture analyses using spring networks with random geometry. *Eng. Frac. Mech.* **1998**, *61*, 569–591. [CrossRef]
11. Berton, S.; Bolander, J.E. Crack band model of fracture in irregular lattices. *Comput. Methods Appl. Mech. Eng.* **2006**, *195*, 7172–7181. [CrossRef]
12. Zhao, G.F.; Yin, Q.; Russell, A.R.; Li, Y.; Li, Y.; Wu, W.; Li, Q. On the linear elastic responses of the 2D bonded discrete element model. *Int. J. Numer. Anal. Met.* **2019**, *43*, 166–182. [CrossRef]

13. Nikolic, M.; Ibrahimbegovic, A.; Miscevic, P. Brittle and ductile failure of rocks: Embedded discontinuity approach for representing mode I and mode II failure mechanisms. *Int. J. Numer. Meth. Eng.* **2015**, *102*, 1507–1526. [CrossRef]
14. Čarija, J.; Nikolic, M.; Ibrahimbegovic, A.; Nikolic, Ž. Discrete softening-damage model for fracture process representation with embedded strong discontinuities. *Eng. Fract. Mech.* **2020**, *236*, 107211. [CrossRef]
15. Rasmussen, L.L.; Assis, A.P. Elastically-homogeneous lattice modelling of transversely isotropic rocks. *Comput. Geotech.* **2018**, *104*, 96–108. [CrossRef]
16. Rasmussen, L.L.; de Farias, M.M.; de Assis, A.P. Extended Rigid Body Spring Network method for the simulation of brittle rocks. *Comput. Geotech.* **2018**, *99*, 31–41. [CrossRef]
17. Simo, J.C.; Oliver, J.; Armero, F. An analysis of strong discontinuities induced by strain-softening in rate-independent inelastic solids. *Comput. Mech.* **1993**, *12*, 277–296. [CrossRef]
18. Ibrahimbegovic, A. *Nonlinear Solid Mechanics: Theoretical Formulations and Finite Element Solution Methods*; Springer: London, UK, 2009.
19. Fang, Y.; Nguyen, B.N.; Carroll, K.; Xu, Z.; Yabusaki, S.B.; Scheibe, T.D.; Bonneville, A. Development of a coupled thermo-hydro-mechanical model in discontinuous media for carbon sequestration. *Int. J. Rock Mech. Min. Sci.* **2013**, *62*, 138–147. [CrossRef]
20. Bažant, Z.P.; Belytschko, T.; Chang, T.P. Continuum theory for strain softening. *J. Eng. Mech.* **1984**, *110*, 1666–1692. [CrossRef]
21. Pijaudier-Cabot, G.; Bažant, Z.P. Nonlocal damage theory. *J. Eng. Mech.* **1987**, *113*, 1512–1533. [CrossRef]
22. Kachanov, L. Time of the rupture process under creep conditions. *TVZ Akad. Nauk. S.S.R. Otd. Tech. Nauk.* **1958**, *8*, 26–31.
23. Lemaitre, J.; Chaboche, J. Aspect phénoménologique de la rupture par endommagement. *J. Mech. App.* **1978**, *2*, 317–365. (In French)
24. Geelen, R.J.M.; Liu, Y.; Hu, T.; Tupek, M.R.; Dolbow, J.E. A phase-field formulation for dynamic cohesive fracture. *Comput. Method. Appl. Mech.* **2019**, *348*, 680–711. [CrossRef]
25. Moes, N.; Belytschko, T. Extended finite element method for cohesive crack growth. *Eng. Fract. Mech.* **2002**, *69*, 813–833. [CrossRef]
26. Belytschko, T.; Chen, H.; Xu, J.; Zi, G. Dynamic crack propagation based on loss of hyperbolicity and a new discontinuous enrichment. *Int. J. Numer. Meth. Eng.* **2003**, *58*, 1873–1905. [CrossRef]
27. Armero, F.; Linder, C. Numerical simulation of dynamic fracture using finite elements with embedded discontinuities. *Int. J. Fract.* **2009**, *160*, 119–141. [CrossRef]
28. Linder, C.; Armero, F. Finite elements with embedded strong discontinuities for the modeling of failure in solids. *Int. J. Numer. Meth. Eng.* **2007**, *72*, 1391–1433. [CrossRef]
29. Alfaiate, J.; Simone, A.; Sluys, L.J. Non-homogeneous displacement jumps in strong embedded discontinuities. *Int. J. Solids Struct.* **2003**, *40*, 5799–5817. [CrossRef]
30. Zhang, Y.; Lackner, R.; Zeiml, M.; Mang, H.A. Strong discontinuity embedded approach with standard SOS formulation: Element formulation, energy-based crack tracking strategy, and validations. *Comput. Methods Appl. Mech. Eng.* **2015**, *287*, 335–366. [CrossRef]
31. Oliver, J.; Huespe, A.E.; Sanchez, P.J. A comparative study on finite elements for capturing strong discontinuities: E-FEM vs. X-FEM. *Comput. Methods Appl. Mech. Eng.* **2006**, *195*, 4732–4752. [CrossRef]
32. Nikolic, M.; Ibrahimbegovic, A. Rock mechanics model capable of representing initial heterogeneities and full set of 3D failure mechanisms. *Comput. Methods Appl. Mech. Eng.* **2015**, *290*, 209–227. [CrossRef]
33. Karavelic, E.; Nikolic, M.; Ibrahimbegovic, A.; Kurtovic, A. Concrete meso-scale model with full set of 3D failure modes with random distribution of aggregate and cement phase. Part I: Formulation and numerical implementation. *Comput. Methods Appl. Mech. Eng.* **2019**, *344*, 1051–1072. [CrossRef]
34. Nikolic, M.; Do, X.N.; Ibrahimbegovic, A.; Nikolic, Z. Crack propagation in dynamics by embedded strong discontinuity approach: Enhanced solid versus discrete lattice model. *Comput. Methods Appl. Mech. Eng.* **2018**, *340*, 480–499. [CrossRef]
35. Nikolic, M. Discrete element model for the failure analysis of partially saturated porous media with propagating cracks represented with embedded strong discontinuities. *Comput. Methods Appl. Mech. Eng.* **2022**, *390*, 114482. [CrossRef]
36. Rizvi, Z.H.; Nikolic, M.; Wuttke, F. Lattice element method for simulations of failure in bio-cemented sands. *Granul. Matter* **2019**, *21*, 18. [CrossRef]
37. Placidi, L.; Timofeev, D.; Maksimov, V.; Barchiesi, E.; Ciallella, A.; Misra, A.; dell'Isola, F. Micro-mechano-morphology-informed continuum damage modeling with intrinsic 2nd gradient (pantographic) grain–grain interactions. *Intern. J. Solids Struct.* **2022**, *254*, 111880. [CrossRef]
38. Misra, A.; Placidi, L.; dell'Isola, F.; Barchiesi, E. Identification of a geometrically nonlinear micromorphic continuum via granular micromechanics. *Z. Angew. Math. Phys.* **2021**, *72*, 1–21. [CrossRef]
39. Battista, A.; Rosa, L.; dell'Erba, R.; Greco, L. Numerical investigation of a particle system compared with first and second gradient continua: Deformation and fracture phenomena. *Math. Mech. Solids* **2017**, *22*, 2120–2134. [CrossRef]
40. Giorgio, I. A discrete formulation of Kirchhoff rods in large-motion dynamics. *Math. Mech. Solids* **2020**, *25*, 1081–1100. [CrossRef]
41. Eremeyev, V.A.; Turco, E. Enriched buckling for beam-lattice metamaterials. *Mech. Res. Commun.* **2020**, *103*, 103458. [CrossRef]
42. Taylor, R.L. *FEAP Finite Element Analysis Program*; University of California: Berkeley, CA, USA, 2017.
43. Bindel, D. *MATFEAP—MATLAB Interfaces to the FEAP Finite Element Code*; Cornell Computer Science: New York, NY, USA, 2011.

44. Geuzaine, C.; Remacle, J.F. Gmsh: A three-dimensional finite element mesh generator with built-in pre- and post-processing facilities. *Int. J. Numer. Meth. Eng.* **2009**, *11*, 1309–1331. [CrossRef]
45. Li, X.; Xu, Y. Phase field modeling scheme with mesostructure for crack propagation in concrete composite. *Intern. J. Solids Struct.* **2022**, *234–235*, 111259. [CrossRef]